Local atomic stacking and symmetry in twisted graphene trilayers

Isaac M. Craig[1], Madeline Van Winkle[1], Catherine Groschner[1], Kaidi Zhang[1], Nikita Dowlatshahi[1], Ziyan Zhu[2], Takashi Taniguchi[3], Kenji Watanabe[4], Sinéad M. Griffin[5,6], and D. Kwabena Bediako[1,7,*]

[1]*Department of Chemistry, University of California, Berkeley, CA 94720, USA*
[2]*SLAC National Accelerator Laboratory, Stanford, CA, USA*
[3]*International Center for Materials Nanoarchitectonics, National Institute for Materials Science, 1-1 Namiki, Tsukuba 305-0044, Japan*
[4]*Research for Functional Materials, National Institute for Materials Science, 1-1 Namiki, Tsukuba 305-0044, Japan*
[5]*Molecular Foundry, Lawrence Berkeley National Laboratory, Berkeley, CA 94720, USA*
[6]*Materials Sciences Division, Lawrence Berkeley National Laboratory, Berkeley, CA 94720, USA*
[7]*Chemical Sciences Division, Lawrence Berkeley National Laboratory, Berkeley, CA 94720, USA*
[*]*Correspondence to: bediako@berkeley.edu*

Abstract

Moiré superlattices formed from twisting trilayers of graphene are an ideal model for studying electronic correlation, and offer several advantages over bilayer analogues, including more robust and tunable superconductivity and a wide range of twist angles associated with flat band formation. Atomic reconstruction, which strongly impacts the electronic structure of twisted graphene structures, has been suggested to play a major role in the relative versatility of superconductivity in trilayers. Here, we exploit an interferometric 4D-STEM approach to image a wide range of trilayer graphene structures. Our results unveil a considerably different model for moiré lattice relaxation in trilayers than that proposed from previous measurements, informing a thorough understanding of how reconstruction modulates the atomic stacking symmetries crucial for establishing superconductivity and other correlated phases in twisted graphene trilayers.

Since their discovery, graphene-based moiré superlattices have proven extraordinarily useful for exploring the interplay between crucial parameters in strongly correlated materials [1–5]. The advantage of these systems lies in the ability to realize a disparate set of physical phenomena through adjusting carrier density, layer number, and interlayer stacking. Trilayer graphene in particular, displays profoundly different physics with different local stacking arrangements [6–9]. Bernal trilayer graphene (ABA stacking) is a semi-metal with a tunable band overlap [10], and contains a band structure containing poorly coupled bands resembling a superimposition of that of monolayer and bilayer graphene. Rhombohedral trilayer graphene (ABC stacking), which differs from the Bernal analogue by only a uniform translation of one layer, instead displays hybridization between all three layers and properties such as metallic behavior [11], Mott insulating states [12], and superconductivity [13]. Differences in lattice symmetry have been proposed to play a large role in the disparate correlated physics of few-layer graphene systems, both in these high symmetry Bernal and rhombodedral structures, and within the locally ordered domains of twisted structures more generally [14, 15].

In particular, previous work has suggested that the flat-bands in twisted bilayer graphene (TBLG) are a fragile topological phase protected by the space-time $C_{2z}T$ inversion symmetry [16, 17]. This protection is maintained although the atomic lattice is only locally inversion symmetric where the carbon atoms of each layer are vertically aligned (AA stacking) [18]. Further, the overlap between flatband states localized within these AA regions (and therefore also the size of AA stacking regions) is thought to play a large role in the superconducting current and transition temperature of moiré systems [19]. The flat-bands responsible for correlated phenomena in twisted graphene multi-layers also appear to rely on this same $C_{2z}T$ symmetry [20]. Like their bilayer analogues, twisted trilayer graphene (TTLG) structures are only locally inversion symmetric about pockets of AAA-type stacking. Results showing that superconductivity in magic angle twisted trilayer graphene (MATTLG) is more robust than in bilayers [21–24] have therefore prompted questions regarding the different roles spontaneous lattice relaxation (also termed atomic reconstruction) may play in these two systems.

In particular, prior imaging has shown that atomic reconstruction in TBLG decreases the relative portion of AA stacking [25, 26]. It has been proposed that atomic relaxation in trilayers may instead increase the portion of inversion symmetric stackings [27], motivating precise characterization of twisted graphene trilayers structures and the general mechanism by which they reconstruct.

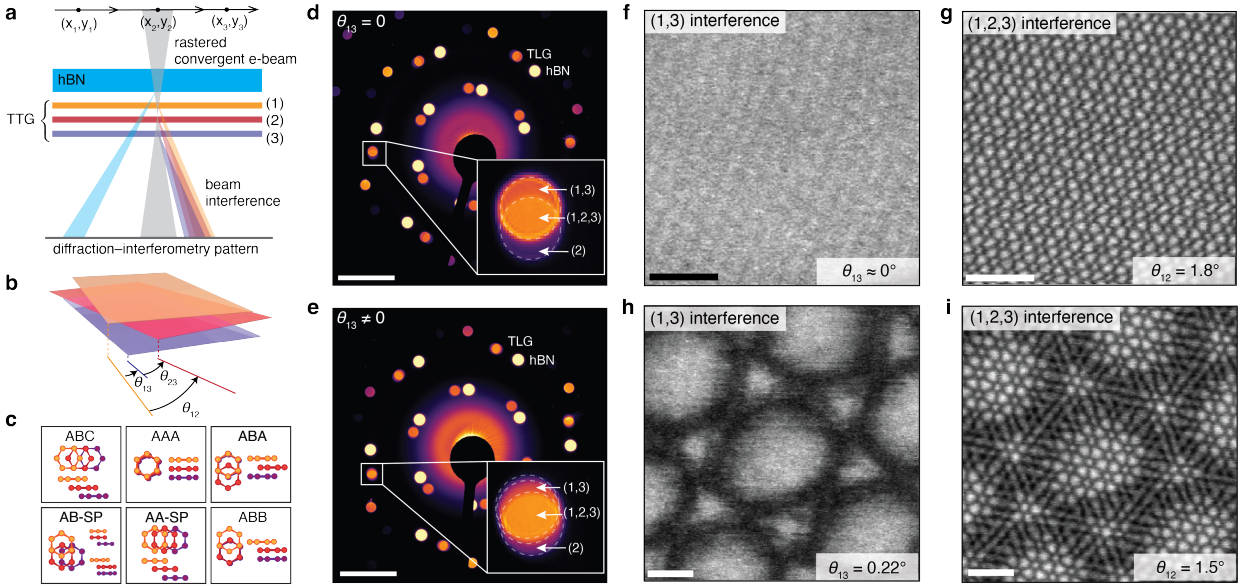

Figure 1: Interferometric 4D-STEM dark field imaging of selected interfaces. (**a**) Schematic of the 4D-STEM approach, wherein beam interference is used to extract stacking order. (**b**) Schematic illustrating the twist angle, θ, and layer numbering conventions used to label the graphene trilayers. (**c**) Illustrations of various high-symmetry stacking configurations realized within twisted trilayer moirés. (**d,e**) Average convergent beam electron diffraction patterns for trilayers with $\theta_{13} \approx 0°$ **(d)** and $\theta_{13} = 0.22^{\circ}$ **(e)**. Overlapping TTLG Bragg disks are highlighted in the insets. Attribution of each Bragg disk to a layer is motivated in SI section 6. **(f,h)** Virtual dark field images corresponding to the overlap of layers 1 & 3. **(g,i)** Virtual dark field images corresponding to the overlap of all three layers. Scale bars are 1 nm^{-1} and 25 nm for reciprocal (**d,e**) and real space (**f–i**), respectively.

Here, we use a four-dimensional scanning transmission electron microscopy, 4D-STEM [28], methodology termed Bragg interferometry (Fig. 1A) that exploits local interference patterns from diffracted electron beams to precisely determine the stacking orientation of atomic layers [26, 29, 30]. This technique not only allows us to probe moiré patterns within encapsulated materials, difficult in scanning tunneling microscopy (STM) as well as other STEM approaches, but further allows us to selectively map the stacking orientation of individual bilayer interfaces within complex multilayered materials. These results provide a direct

measure of the local stacking within the material. We find that the results of this 4D-STEM measurement suggest a picture of reconstruction that is markedly different from that proposed by previous STM work [27], and one that is consequential for understanding the correlated electron physics in these materials.

The interferometric 4D-STEM technique we use involves scanning a converged electron beam across the sample of interest and collecting individual diffraction patterns for each real space position of the probe (Fig. 1A). Throughout this work, we use the notation shown in Fig. 1B to label the twist angles, θ, within the trilayer sample. Here, θ_{12} and θ_{23} denote the twist angles between layers 1 & 2, and layers 2 & 3 respectively such that $\theta_{13} = \theta_{12} + \theta_{23}$. We further use the labels shown in Fig. 1C to denote the various high symmetry stacking configurations realized within the moiré. The converged beam electron diffraction (CBED) patterns collected at each probe location then appear as shown in Figs. 1D,E, where each layer of the material generates a set of Bragg disks. The overlap between Bragg disks originating from different layers (inset Figs. 1D,E) is then used to determine the stacking orientation of those two layers. As an example, Figs. 1F,H show how the intensity of the overlap between layers 1 and 3—denoted as '(1,3) overlap'—varies across the sample. This modulation in intensity directly manifests the moiré pattern between layers 1 and 3 but is insensitive to the orientation of the second layer. Similarly the variation in the intensity of the (1,2,3) overlap region (Figs. 1G,I) reveals the modulation in stacking order between all three graphene layers.

Therefore, by exploiting the relationship between stacking order and overlap region intensity (see SI sections 7–9), we map the variation in atomic stacking and hence reconstruction within trilayer graphene samples. Results of these analyses are shown in Fig. 2 for a structure that we call 'AtA' in which the top and bottom graphene layers are perfectly aligned to each-other and twisted with respect to the middle layer (Fig. 2B). In this structure, the average intensity of the overlap regions in the first ring of Bragg reflections and the average overlap region intensity in the second ring of reflections can be used to determine the local stacking configuration. Using the bi-variate color-legend shown in Fig. 2A (in which the

high symmetry stacking configurations associated with each color are overlaid), we create a map of local atomic stacking within an AtA sample (Fig. 2C).

The local atomic stacking shown in Fig. 2C indicates that this particular AtA sample for which ($\theta_{12} = 1.05°$) relaxes to decrease the total amount of AAA stacking (white) when compared to the stacking order distribution in a rigid AtA trilayer (Fig. 2E). This is expected as AAA stacking is roughly 29.5 and 36.5 meV/unit cell higher in energy than A-SP-A and ABA stacking respectively (See SI section 13). Further, the histogram shown (Fig. 2D) illustrates that this sample contains considerably more ABA, BAB, and SP type stacking than AAA type stacking (See SI figure 3 for the stacking histogram expected of a rigid sample). This reconstruction also manifests in the mean line-cut shown in Fig. 2F, which corresponds to the average over all line-cuts equivalent to that denoted by the dotted line in Fig. 2C. From this profile, it is evident that the widths of the AAA regions are smaller than expected for a rigid trilayer, which is robust the presented standard deviation (shaded region) and noise-driven differences in normalization (See SI section 10) as well as and limitations in spatial resolution due to appreciable beam-width biasing (See SI section 9).

These results, as well as results for other twist angles shown in SI section 12, together illustrate that AtA trilayers show an observably reconstructed atomic stacking distribution up to a at least a twist angle of 1.81°, with few differences seen between the 1.81° and 1.0° samples. We also observe that the AtA trilayers show a pattern of reconstruction similar to that of a twisted bilayer within this twist angle range [25, 26], although a more quantitative comparison between the bilayer and AtA trilayer reconstruction necessitates more detailed intensity fitting approach to map strain tensor fields [26, 29] and will be addressed in future work.

A similar analysis is carried out for samples which we refer to as 'tAB', in which the bottom two graphene layers are aligned AB and the top layer is twisted (Fig. 2H), creating a structure sometimes referred to as a 'monolayer-on-bilayer graphene', which also exhibits correlated electron physics [31, 32]. Unlike the AtA trilayers, these tAB structures show

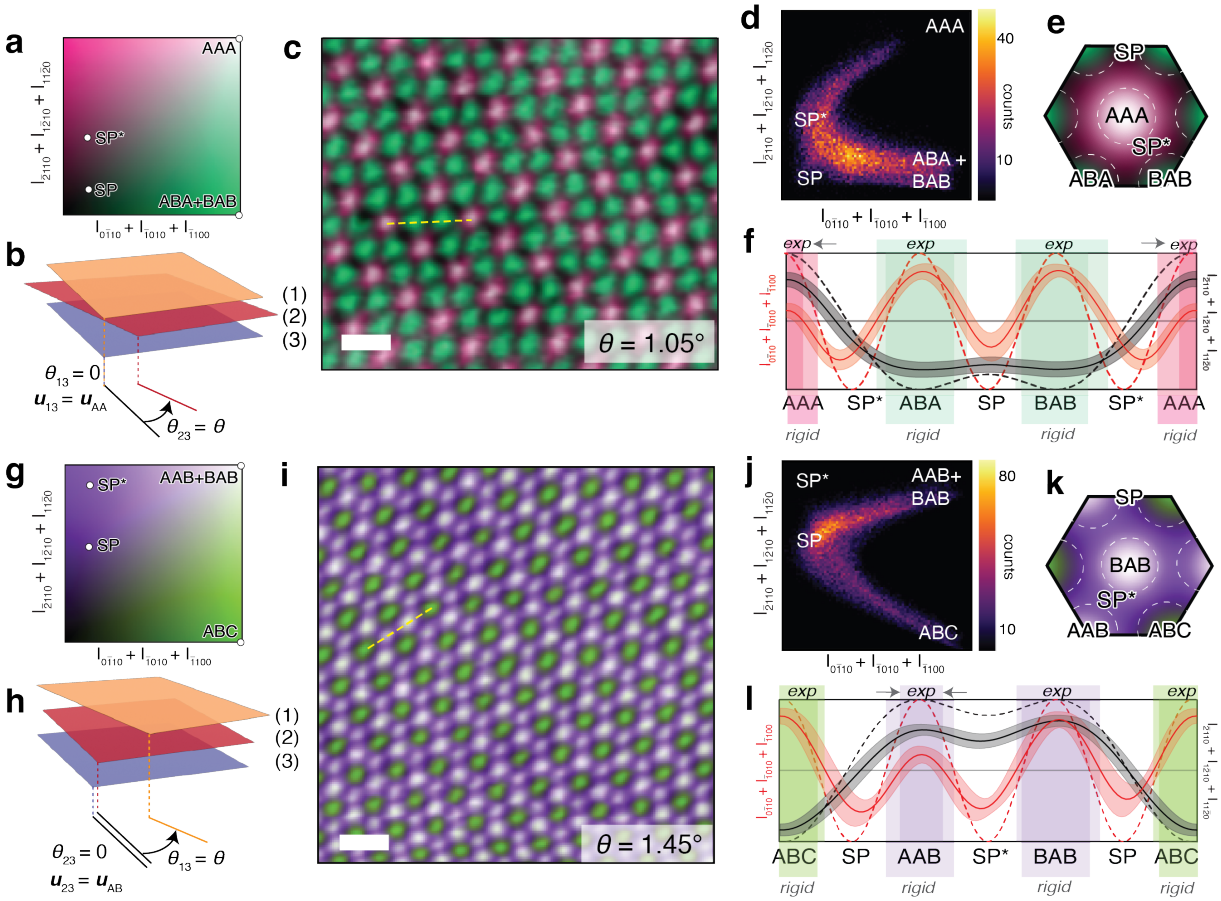

Figure 2: Reconstruction in AtA and tAB trilayers. (**b, h**) schematic illustrating the layer alignment in a AtA and a tAB trilayer. (**a, g**) Legends illustrating how color correlates with the average first and second order Bragg disks intensities. Overlaid points are the intensities of high symmetry stacking orders obtained via multislice, see Methods. (**c, i**) Maps of local stacking order for AtA and tAB trilayers, cropped to exclude biasing from sample drift. (**d, j**) Histograms illustrating the relative prevalence of each stacking configuration. Note that since the intensity does not depend linearly on the stacking order, a rigid bilayer will not display a uniform distribution of intensities (see SI section 7). (**e, k**) Schematics illustrating the anticipated variation in local stacking order expected for a rigid structure, obtained via the expressions provided in SI section 7. The convention is used that AAA, ABA, SP, and SP* stacking denote interlayer offsets of $u_{12} = (0,0), (a_0/\sqrt{3}, 0), (a_0(2\sqrt{3})^{-1}, 0)$, and $(0, a_0/2)$ respectively in Cartesian coordinates where a_0 is the lattice constant. Similarly for the tAB samples, AAA, ABC, SP, and SP* stacking denote interlayer offsets of $u_{13} = (0,0), (a_0/\sqrt{3}, 0), (a_0(2\sqrt{3})^{-1}, 0)$, and $(0, a_0/2)$ respectively. (**f, l**) Intensity line-cuts corresponding to the average of all possible line-cuts equivalent to the dotted lines shown in (**c, i**) are given as solid lines. Shaded region represents the standard deviation and arrows denote the statistically significant contractions of AAA and AAB domains. Intensity variation expected for a rigid structure are given as dotted lines. Domain sizes are calculated from the full width at half max of $I_{0\bar{1}10} + I_{\bar{1}010} + I_{\bar{1}100}$ (red) as highlighted, where the value of $I_{\bar{2}110} + I_{1\bar{2}10} + I_{11\bar{2}0}$ (black) is used to distinguish between different high symmetry stacking orders (see SI Section 9 for validation of this approach). All scale bars are 25 nm.

atomic reconstruction patterns driven by a preference to decrease the relative portion of AAB stacking, as seen by comparing Fig. 2I to the rigid stacking order distribution (Fig. 2K), the histogram in Fig. 2J, and the corresponding line-cut in Fig. 2L (see SI section 9 for normalization bias and error margins), which illustrates the tAB structure reconstructs such that the portions of AAB and BAB stacking are no longer equivalent as they would be in a rigid moiré. This decrease in AAB stacking is expected, it is 17.9 meV/unit cell higher in energy than ABC and BAB (See SI section 13). We note here that this manifests in the AAB regions appearing to have a lower peak $I_{0\bar{1}10}+I_{\bar{1}010}+I_{\bar{1}100}$ intensity to the BAB regions, while these regions are expected to appear sharper but with similar maximum intensity. This is likely due to broadening from a number of factors associated with measurement acquisition and post-processing, especially the beam-width biasing and the Gaussian filter used (see SI section 9).

The observation that AAB and BAB regions are observably distinct even at a twist angle of 1.4° is nonetheless notable. This effect is more dramatic at smaller twist angles as seen in the stacking order percent area trends and maps gathered within the 0.1° – 1.5° twist angle regime (see SI Section 12). While the approach used in this work prohibits a quantitative comparison of the AAB and BAB domain sizes (to be addressed in future work), these results still clearly establish that the size of ABC and BAB domains are comparable to each-other and much larger than the AAB domains. Moreover, the stacking order distributions seen for tAB appear similar to those observed in twisted bilayer graphene [26], suggesting that atomic reconstruction in tAB trilayer samples can be explained primarily from consideration of the twisted interface.

The results discussed thus far concern a limiting case of graphene trilayers wherein two of the layers are perfectly aligned. While these materials are conceptually simpler and display rich physical properties which merit their investigation, this interferometric 4D-STEM technique also permits us to study a broader array of twisted trilayer structures with two independent twist angles. In these more complex multilayered samples, the ability to selectively probe buried bilayer interfaces allows us to independently image the larger scale moiré pattern and

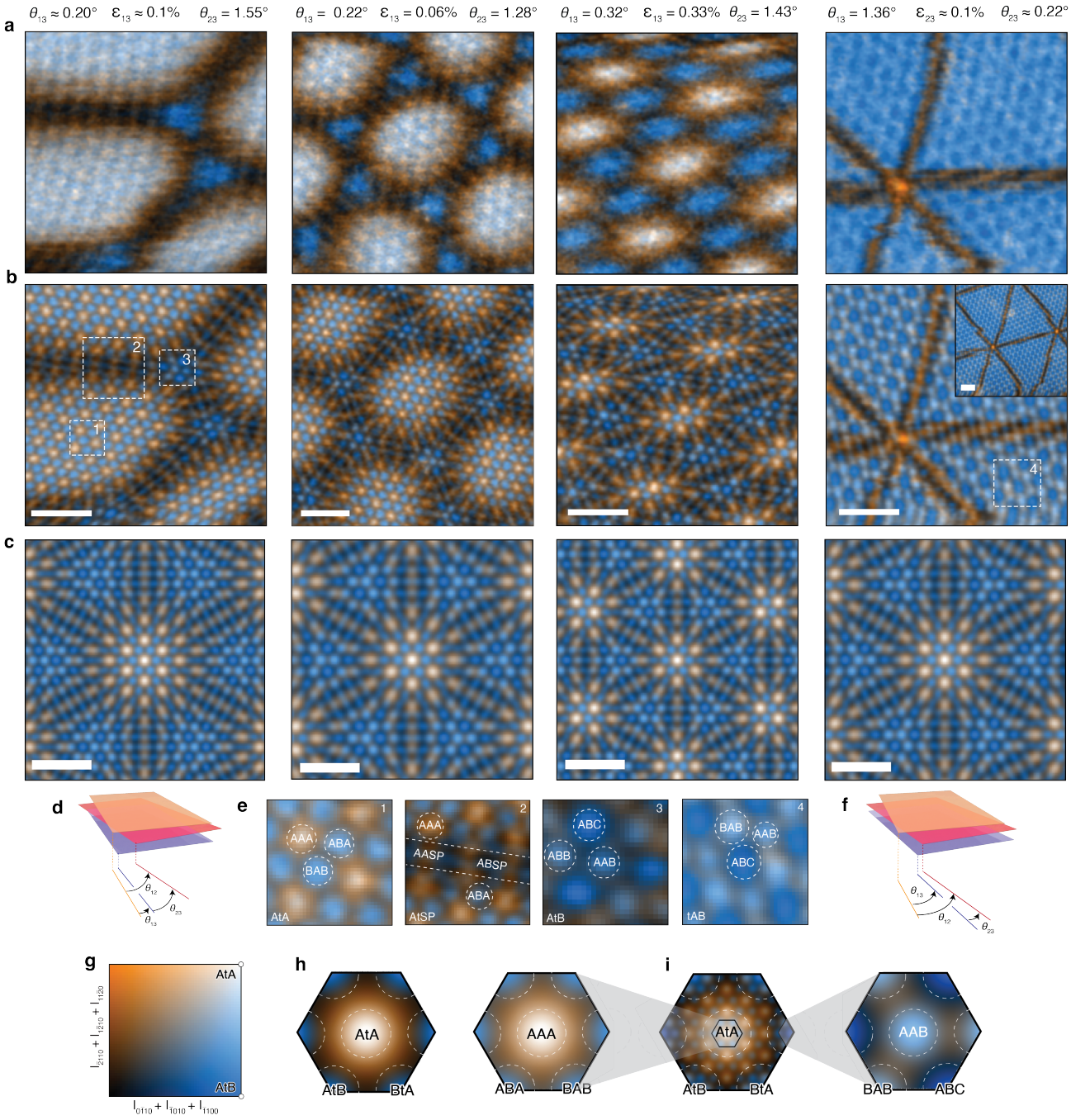

Figure 3: Atomic Stacking in slightly misaligned TTLG. (**a**) Maps of local atomic stacking from the larger moiré pattern only, corresponding to the local in-plane offset between between layers 1 and 3 in panels 1-3, and the local in-plane offset between layers 2 and 3 in panel 4. Colors shown correspond to the bi-variate colormap in (**g**), with accompanying expressions and simulations motivating the attribution of intensities to stacking orders as labeled here in SI sections 7-9. (**b**) Local atomic stacking obtained from considering all three graphene layers. (**c**) Simulated stacking order maps for rigid moiré superlattice analogues of **b**, obtained from the expression given in SI Section 8. All scale bars are 25 nm. (**d,f**) Schematics of layer alignment in TTLG with slightly misaligned layers. (**e**) Zoom-ins of the maps above illustrating the finer local modulation of stacking order within (**1**) AtA, (**2**)

AtSP, (**3**) AtB, and (**4**) tAB regions. (**g**) Legend illustrating how color correlates with the average first and second order Bragg disks intensities for both the two and three layer interference patterns, with labeled locations of two layer high symmetry regions. **(h)** The expected intensity variation for an individual bilayer interface within the general trilayer structure obtained via the expression provided in SI section 7. **(i)** Variation in first and second order Bragg disks intensities expected for a rigid twisted trilayer obtained via the expression provided in SI section 8. Intensity relations are verified with multi-slice simulations in SI section 9.

evaluate its effect on local stacking order.

Following this approach, we extract stacking order maps associated with the larger moiré pattern from double overlap (Fig. 3A) and triple overlap (Fig. 3B,E). These are compared to the maps calculated for rigid moirés in Fig. 3C. For the the double overlap case, Fig. 3A reveals the presence of large local regions in which two layers are aligned directly atop each-other (AtA or tAA, white) and regions in which two layers are aligned AB (AtB or tAB, blue). From comparing the stacking distributions of samples with $0 < \theta_{13} \ll \theta_{23}$ (three leftmost panels in Fig. 3A, illustrated in Fig. 3D) and $0 < \theta_{23} \ll \theta_{13}$ (rightmost panel in Fig. 3A, illustrated in Fig. 3F), we find that the two regimes display distinct reconstruction patterns. When $\theta_{13} \ll \theta_{23}$, the observed atomic reconstruction is driven by a slight preference for AtA type stacking (white) over AtB (blue) and soliton-type (grey) regions. This result is somewhat unexpected as the energetic difference between rigid AtA and AtB domains (driven only by inter-layer coupling between the top and bottom layers) has been previously presumed to play a minor role in reconstruction [33]. Moreover, previous STM studies [27] concluded that trilayers with $0 < \theta_{13} \ll \theta_{23}$ relaxed to effectively eliminate AtB domains.

Fig. 3A also shows (rightmost panel) that the atomic reconstruction pattern for $\theta_{23} \ll \theta_{13}$ is instead driven by a preference to minimize the high energy tAA (white) domains, within which every possible stacking configuration must place two carbon atoms from neighboring layers directly atop each other — an arrangement that is sterically unfavorable [25, 26]. The extent of reconstruction in these $\theta_{23} \ll \theta_{13}$ samples is therefore much larger, since the energy difference between rigid tAA vs tAB domains ($\approx$ 18.2 meV/unit when considering only adjacent interfaces) is much larger than that between rigid AtA vs AtB domains ($\approx$

0 meV/unit when considering only adjacent interfaces) [23, 33]. This is reflected in the difference between the structures shown in the second and fourth columns of Fig. 3, in which both structures have comparable twist angles, but the structure in the fourth panel is observably more reconstructed, with the tAA domains appearing as a highly contracted spot. This spot appears orange rather than white due to beam-width and data processing effects (see SI section 9). Although the weaker higher frequency texture observed within the white and blue domains in Fig. 3A might arise from the smaller scale moiré pattern imparting a modulation in these stacking distributions, this pattern likely predominantly results from a small bleed-in of the (1,2,3) interference pattern, which is hard to completely exclude with virtual apertures while retaining sufficient signal-to-noise ratios.

After extracting the local AtA/tAA and AtB/tAB domains as shown in Fig. 3A, we now examine the (1,2,3) overlap region, which is associated with all three graphene layers (Figs. 3B), to understand how the smaller scale moiré pattern modulates local stacking order within these larger domains (representative regions of these maps are magnified in Fig. 3E). Additional maps are shown in SI Figs. 7-8. We note that, as noted in previous work [27], we see only two clear periodicities in our data despite the presence of three moiré wavelengths from each twisted bilayer interface. However, this does not necessarily imply that only two moiré wavelengths are present; inspection of the atomic stacking maps expected from even rigid structures (Fig. 3C and SI Figures 7-8) reveals that the smaller and larger periodicities observed reflect only the largest and smallest twist angles, respectively.

Taken together, the data in Fig. 3 allow a quantification of the area fractions in TTLG samples and the development of a qualitative model for reconstruction in the limit of slight misalignment (Fig. 4). Fig. 4A shows that for the larger moiré pattern, the proportion of AtA/tAA and AtB/tAB stacking domains inverts across the regimes illustrated in Figs. 3D,F. Associated area fractions from our measurements and those from continuum relaxation simulations as a function of $\theta_{13} - \theta_{23}$ are shown in Fig. 4A. Experiment and simulation show good agreement in the overall trends, though the measurements show a more gradual decline in area fraction of AtA/tAA (and corresponding rise in that of AtB/tAB/SP) than the

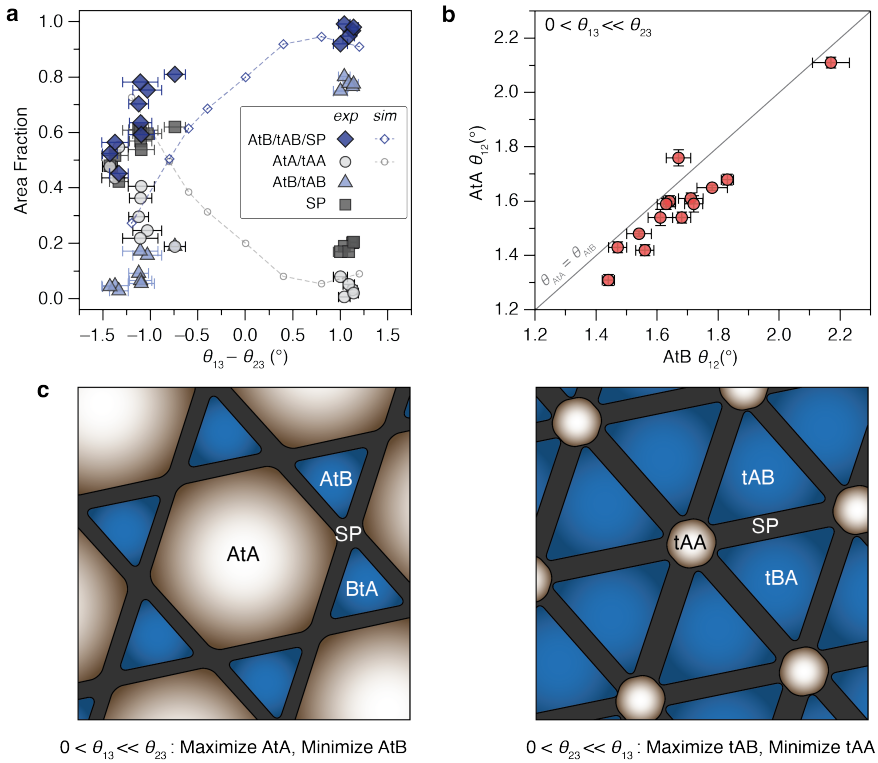

Figure 4: Reconstruction patterns and trends in TTLG. (**a**) Area fraction of atomic stacking domains from the larger moiré pattern only as a function of $\theta_{13} - \theta_{23}$. As both θ_{13} and θ_{23} are slightly variable for the samples discussed, additional plots of area fraction against θ_{13} and θ_{23} independently are provided in SI Fig. 10. Experimental (*exp*) data (corresponding to the maps shown in Fig. 3 and SI Figs. 7-8) are compared with relaxation simulations (*sim*). Area fractions associated with the experimental and simulated data were obtained following the procedure outline in SI section 11 (with regions of $I_{0\bar{1}10} + I_{\bar{1}010} + I_{\bar{1}100}$ > 0.5 and $I_{\bar{2}110} + I_{1\bar{2}10} + I_{11\bar{2}0} < 0.5$ labeled AtB/tAB, $I_{0\bar{1}10} + I_{\bar{1}010} + I_{\bar{1}100} > 0.5$ and $I_{\bar{2}110} + I_{1\bar{2}10} + I_{11\bar{2}0} > 0.5$ labeled AtA/tAA, and those remaining SP) and by applying a threshold of 0.25 degrees to the local curl respectively (with further details in SI section 13). We note that these methods result in functionally equivalent categorizations due to the small area and large intensity variation associated with the soliton regions where these thresholds partition the data. (**b**) Local twist angle associated with the smaller moiré within AtA and AtB domains. All points correspond to the regime where $\theta_{13} \ll \theta_{23}$. Twist angle determination is described in SI section 5. (**c**) Qualitative schematic illustrating the atomic reconstruction patterns (large moiré) observed for $\theta_{13} \ll \theta_{23}$ and $\theta_{23} \ll \theta_{13}$.

simulation with increasing $\theta_{13} - \theta_{23}$. This slight discrepancy may arise because of kinetic effects preventing the system from realizing the theoretically optimal extent of relaxation driven by layers not immediately adjacent.

For the smaller scale moiré superlattice, we find that this pattern appears relatively invariant within the AtA, AtSP, AtB, and tAB domains (SI Section 12). Indeed, the measured proportion of stacking orders within the AtA regions of Fig. 3 is very similar to the pure AtA sample seen in Fig. 2C, suggesting that the larger scale moiré plays a relatively minor role in the reconstruction of the smaller scale moiré. We do however observe some differences between the smaller-scale moiré within different domains. As shown in Fig. 4B, measurements of local θ_{12} values within the AtA and AtB domains of $\theta_{13} \ll \theta_{23}$ samples display a slightly smaller θ_{12} angle within AtA regions as compared to the values in adjacent AtB domains. This tightening of the smaller-scale moiré within AtB regions might help facilitate the overall minimization of these AtB regions.

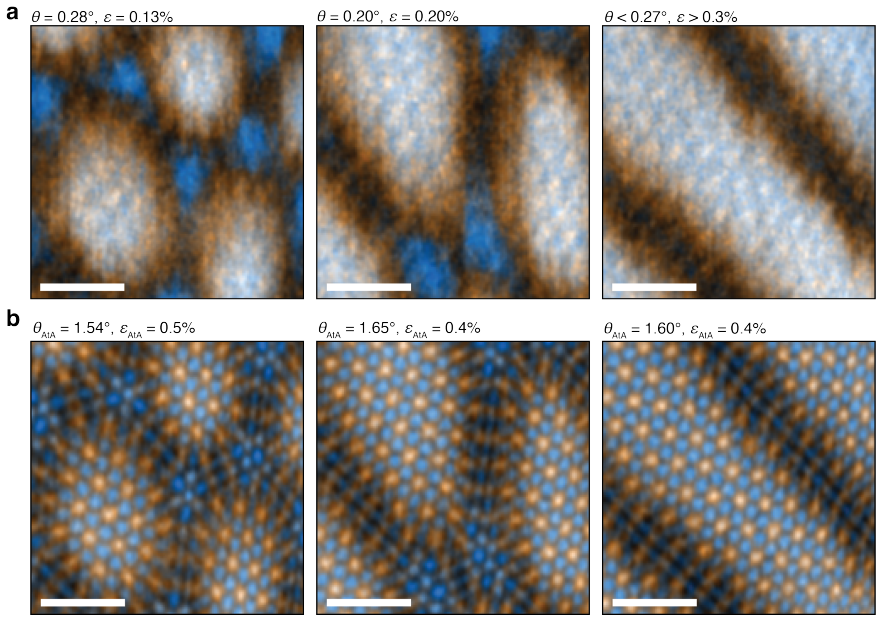

Figure 5: Heterostrain Effects (**a**) Maps of the modulation in local stacking order between layers 1 and 3 only for samples with an increasingly large percent of extrinsic heterostrain. (**b**) Corresponding maps of the local stacking order modulation obtained when considering all three graphene layers. Twist angles and percent heterostrains values and bounds were determined from fitting the size and asymmetry of the moiré triangles (see SI section 5). All scale bars are 25 nm.

Lastly, we investigate the maps of local atomic stacking order in regions with an increasingly

large extent of extrinsic heterostrain, ϵ (obtained via the procedure outlined in SI section 5). From the maps shown in Fig. 5, we find that extrinsic heterostrain acts predominantly on the larger scale moiré pattern and has a diminishing effect on the smaller scale moiré superlattice, consistent with previous work on bilayer moiré systems [26, 29]. Notably, in the most heterostrained sample of Fig. 5, despite similar θ_{13}, the islands of AtA are deformed into stripes. These features have also been previously visualized in STM studies and attributed to heterostrain between the top and bottom layers [23]. Heterostrain is therefore a powerful tuning knob for manipulating the contiguity of AtA domains (from islands to stripes) at the expense of AtB regions, potentially modulating the emergence of correlated phases that rely on the $C_{2z}T$-symmetric AtA domains.

In conclusion, the nature of atomic reconstruction unveiled here for twisted trilayers is markedly different than that proposed in previous work, wherein it was suggested that slightly misaligned MATTLG samples relax to almost exclusively AtA regions, with the AtB and SP regions stretched into thin domain boundaries and/or topological defects that contribute insignificantly to the STM measurements [27]. While Fig. 2 shows that at length scales where only one moiré wavelength is apparent (when $\theta_{13} \approx 0°$), trilayers do favor the formation of large AtA domains, and in that case the local structure of trilayers is driven primarily by consideration of the smaller moiré, we see a clear presence of considerable AtB type stacking down to $\theta_{13} = 0.20°$ (Fig. 3). This observation contrasts previous claims of trilayer samples containing contributions from only AtA regions at a θ_{13} of $\approx 0.25°$, with further discussion of our results in the context of these prior measurements provided in SI section 14. Taken together, our measurements highlight the particular utility of interferometric 4D-STEM imaging alongside other scanning probe techniques like STM for characterizing complex multi-layered moirés, as the ability to apply a direct structural probe selectively to separate interfaces can uncover the complex picture of atomic reconstruction.

The extent of AtB stacking observed could have major implications for understanding superconductivity in misaligned MATTLG [22, 23] and recently discovered moiré quasicrystal systems [34]. For instance, if $\theta_{13} \ll \theta_{23}$ configurations such as MATTLG favored entirely

AtA stacking as previously proposed, their correlated behaviors could be predominantly understood by consideration of the $C_{2z}T$ inversion symmetric AAA stacking regions much like TBLG. While our measurements support a relative contraction of AtB domains, it is no where near as dramatic, revealing that sizable AtB portions remain following reconstruction. These significant AtB domains may instead suggest that the ABC, AAB, and ABB regions, which have been shown to host correlated electronic phases [13, 35–37] despite a lack of inversion symmetry, may play an important role in understanding correlated electron physics in some twisted trilayers.

Acknowledgements

We thank P. Kim, J. Ciston, K. Bustillo, and C. Ophus for vis-a-vis and epistolary discussions. This material is based upon work supported by the US National Science Foundation Early Career Development Program (CAREER), under award no. 2238196. I.M.C. acknowledges the NDSEG program for a pre-doctoral fellowship. C.G. was supported by a grant from the W.M. Keck Foundation (Award no. 993922). Experimental work at the Molecular Foundry, LBNL was supported by the Office of Science, Office of Basic Energy Sciences, the U.S. Department of Energy under Contract no. DE-AC02-05CH11231. Confocal Raman spectroscopy was supported by a Defense University Research Instrumentation Program grant through the Office of Naval Research under award no. N00014-20-1-2599 (D.K.B.). Other instrumentation used in this work was supported by grants from the Canadian Institute for Advanced Research (CIFAR–Azrieli Global Scholar, Award no. GS21-011), the Gordon and Betty Moore Foundation EPiQS Initiative (Award no. 10637), and the 3M Foundation through the 3M Non-Tenured Faculty Award (no. 67507585). Theoretical work was supported by the Theory of Materials FWP at Lawrence Berkeley National Laboratory, funded by the U.S. Department of Energy, Office of Science, Basic Energy Sciences, Materials Sciences and Engineering Division, under Contract No. DE-AC02- 05CH11231 (S.G). K.W. and T.T. acknowledge support from JSPS KAKENHI (Grant Numbers 19H05790, 20H00354 and 21H05233).

Author Contributions

I.M.C., M.V., C.G., and D.K.B. conceived the study. M.V., C.G., K.Z., and N.D. fabricated the samples. M.V., C.G., and I.M.C. performed the experiments. I.M.C. and Z.Z. performed the continuum simulations using code developed by Z.Z. I.M.C. developed and implemented the interferometry code (with assistance from C.G.) and analyzed the data. T.T. and K.W. provided the hBN crystals. D.K.B. and S.M.G. supervised the work. I.M.C. and D.K.B. wrote the manuscript with input from all co-authors.

Competing Interests

The authors declare no competing interests.

Data Availability

The data supporting the findings of this study are available within the Article and its Supplementary Information files.

Representative datasets can be found at https://doi.org/10.5281/zenodo.4459669.

Code Availability

The code developed for data analysis in this study is available within the TrilayerTEM sub-directory at https://github.com/bediakolab/bediakolab_scripts.

Additional Information

Correspondence and requests for materials should be emailed to DKB (email: bediako@berkeley.edu).

References

1. Balents, L., Dean, C. R., Efetov, D. K. & Young, A. F. Superconductivity and strong correlations in moiré flat bands. *Nature Physics* **16,** 725–733 (2020).
2. Cao, Y. *et al.* Correlated insulator behaviour at half-filling in magic-angle graphene superlattices. *Nature* **556,** 80–84 (2018).

3. Cao, Y. *et al.* Unconventional superconductivity in magic-angle graphene superlattices. *Nature* **556,** 43–50 (2018).
4. Lau, C. N., Bockrath, M. W., Mak, K. F. & Zhang, F. Reproducibility in the fabrication and physics of moiré materials. *Nature* **602,** 41–50 (2022).
5. Tian, H. *et al.* Evidence for Dirac flat band superconductivity enabled by quantum geometry. *Nature* **614,** 440–444 (2023).
6. Bao, W. *et al.* Stacking-dependent band gap and quantum transport in trilayer graphene. *Nature Physics* **7,** 948–952 (2011).
7. Kumar, A. *et al.* Integer quantum Hall effect in trilayer graphene. *Physical Review Letters* **107,** 126806 (2011).
8. Lui, C. H., Li, Z., Mak, K. F., Cappelluti, E. & Heinz, T. F. Observation of an electrically tunable band gap in trilayer graphene. *Nature Physics* **7,** 944–947 (2011).
9. Yuan, S., Roldán, R. & Katsnelson, M. I. Landau level spectrum of ABA-and ABC-stacked trilayer graphene. *Physical Review B* **84,** 125455 (2011).
10. Craciun, M. *et al.* Trilayer graphene is a semimetal with a gate-tunable band overlap. *Nature nanotechnology* **4,** 383–388 (2009).
11. Zhou, H. *et al.* Half-and quarter-metals in rhombohedral trilayer graphene. *Nature* **598,** 429–433 (2021).
12. Chen, G. *et al.* Evidence of a gate-tunable Mott insulator in a trilayer graphene moiré superlattice. *Nature Physics* **15,** 237–241 (2019).
13. Zhou, H., Xie, T., Taniguchi, T., Watanabe, K. & Young, A. F. Superconductivity in rhombohedral trilayer graphene. *Nature* **598,** 434–438 (2021).
14. Koshino, M. & McCann, E. Gate-induced interlayer asymmetry in ABA-stacked trilayer graphene. *Physical Review B* **79,** 125443 (2009).
15. Morell, E. S., Pacheco, M., Chico, L. & Brey, L. Electronic properties of twisted trilayer graphene. *Physical Review B* **87,** 125414 (2013).
16. Ahn, J., Park, S. & Yang, B.-J. Failure of Nielsen-Ninomiya theorem and fragile topology in two-dimensional systems with space-time inversion symmetry: application to twisted bilayer graphene at magic angle. *Physical Review X* **9,** 021013 (2019).

17. Song, Z. *et al.* All magic angles in twisted bilayer graphene are topological. *Physical review letters* **123,** 036401 (2019).

18. Zou, L., Po, H. C., Vishwanath, A. & Senthil, T. Band structure of twisted bilayer graphene: Emergent symmetries, commensurate approximants, and Wannier obstructions. *Physical Review B* **98,** 085435 (2018).

19. Törmä, P., Peotta, S. & Bernevig, B. A. Superfluidity and quantum geometry in twisted multilayer systems. *arXiv preprint arXiv:2111.00807* (2021).

20. Mora, C., Regnault, N. & Bernevig, B. A. Flatbands and perfect metal in trilayer moiré graphene. *Physical review letters* **123,** 026402 (2019).

21. Park, J. M., Cao, Y., Watanabe, K., Taniguchi, T. & Jarillo-Herrero, P. Tunable strongly coupled superconductivity in magic-angle twisted trilayer graphene. *Nature* **590,** 249–255 (2021).

22. Hao, Z. *et al.* Electric field–tunable superconductivity in alternating-twist magic-angle trilayer graphene. *Science* **371,** 1133–1138 (2021).

23. Kim, H. *et al.* Evidence for unconventional superconductivity in twisted trilayer graphene. *Nature* **606,** 494–500 (2022).

24. Zhang, X. *et al.* Correlated insulating states and transport signature of superconductivity in twisted trilayer graphene superlattices. *Physical review letters* **127,** 166802 (2021).

25. Yoo, H. *et al.* Atomic and electronic reconstruction at the van der Waals interface in twisted bilayer graphene. *Nat. Mater.* **18,** 448–453 (2019).

26. Kazmierczak, N. P. *et al.* Strain fields in twisted bilayer graphene. *Nature materials* **20,** 956–963 (2021).

27. Turkel, S. *et al.* Orderly disorder in magic-angle twisted trilayer graphene. *Science* **376,** 193–199 (2022).

28. Ophus, C. Four-dimensional scanning transmission electron microscopy (4D-STEM): From scanning nanodiffraction to ptychography and beyond. *Microscopy and Microanalysis* **25,** 563–582 (2019).

29. Van Winkle, M. *et al.* Quantitative Imaging of Intrinsic and Extrinsic Strain in Transition Metal Dichalcogenide Moir\'e Bilayers. *arXiv preprint arXiv:2212.07006* (2022).

30. Zachman, M. J. *et al.* Interferometric 4D-STEM for lattice distortion and interlayer spacing measurements of bilayer and trilayer 2D materials. *Small* **17,** 2100388 (2021).

31. Tong, L.-H. *et al.* Spectroscopic visualization of flat bands in magic-angle twisted monolayer-bilayer graphene: coexistence of localization and delocalization. *Physical Review Letters* **128,** 126401 (2022).

32. Park, Y., Chittari, B. L. & Jung, J. Gate-tunable topological flat bands in twisted monolayer-bilayer graphene. *Physical Review B* **102,** 035411 (2020).

33. Zhu, Z., Carr, S., Massatt, D., Luskin, M. & Kaxiras, E. Twisted trilayer graphene: A precisely tunable platform for correlated electrons. *Physical review letters* **125,** 116404 (2020).

34. Uri, A. *et al.* Superconductivity and strong interactions in a tunable moiré quasiperiodic crystal. *arXiv preprint arXiv:2302.00686* (2023).

35. Chen, G. *et al.* Tunable correlated Chern insulator and ferromagnetism in a moiré superlattice. *Nature* **579,** 56–61 (2020).

36. Xu, S. *et al.* Tunable van Hove singularities and correlated states in twisted monolayer–bilayer graphene. *Nature Physics* **17,** 619–626 (2021).

37. Li, S.-y. *et al.* Imaging topological and correlated insulating states in twisted monolayer-bilayer graphene. *Nature Communications* **13,** 1–7 (2022).